Ceramics International 48 (2022) 2012–2020

Contents lists available at ScienceDirect

Ceramics International

journal homepage: www.elsevier.com/locate/ceramint

Fabrication, microstructure and high-temperature plastic deformation of three-phase $Al_2O_3/Er_3Al_5O_{12}/ZrO_2$ sintered ceramics

F.A. Huamán-Mamani [a], C. Jiménez-Holgado [b], M. Jiménez-Melendo [c,*]

[a] Departamento de Ciencias Naturales, Universidad Católica San Pablo, Arequipa, Peru
[b] Department of Chemistry, School of Science, University of Ioannina, 45110, Ioannina, Greece
[c] Departamento de Física de la Materia Condensada, Universidad de Sevilla, 41080, Sevilla, Spain

ARTICLE INFO

Keywords:
Composites
Grain boundaries
Creep
Al_2O_3

ABSTRACT

The fabrication, microstructure and high-temperature creep behavior of chemically compatible, three-phase alumina/erbium aluminum garnet ($Er_3Al_5O_{12}$, EAG)/erbia fully-stabilized cubic ZrO_2 (ESZ) particulate composites with the ternary eutectic composition is investigated. The composites were fabricated by a solid-state reaction route of α-Al_2O_3, Er_2O_3 and monoclinic ZrO_2 powders. The final phases α-Al_2O_3, EAG and ESZ were obtained after calcination of the powder mixtures at 1400 °C. High dense bulk composites were obtained after sintering at 1500 °C in air for 10 h, with a homogeneous microstructure formed by fine and equiaxed grains of the three phases with average sizes of 1 μm. The composites were tested in compression at temperatures between 1250 and 1450 °C in air at constant load and at constant strain rate. As the temperature increases, a gradual brittle-to-ductile transition was found. Extended steady states of deformation were attained without signs of creep damage in the ductile region, characterized by a stress exponent of nearly 2 and by the lack of dislocation activity and modifications in grain size and shape. The main deformation mechanism in steady state is grain boundary sliding, as found in superplastic metals and ceramics. In the semibrittle region, microcavities developed along grain boundaries; these flaws, however, did not grow and coalescence into macrocracks, resulting in a flaw-tolerant material. Alumina is the creep-controlling phase in the composite because of the grain boundary strengthening caused by the (unavoidable) Er^{3+}- and Zr^{4+}-doping provided by the other two phases.

1. Introduction

Oxide ceramics are currently used in structural applications, particularly at elevated temperatures owing to their superior chemical and thermal stability and excellent mechanical behavior, such as creep resistance. In particular, alumina-based compounds are probably the most used engineering oxide ceramics nowadays. Though pure monolithic alumina is inherently brittle, exhibiting low fracture toughness at room and high temperatures [1,2], its mechanical properties can be considerably improved by the incorporation of additional phases (fibers, particulates, layers, etc.) in composite structures. For example, dual phase Al_2O_3/ZrO_2 (zirconia-toughened alumina, ZTA) particulate composites have been shown to exhibit better stability and mechanical properties at low and high temperatures than the single-phase constituents [3–6]. Similarly, the two–phase Al_2O_3/yttrium aluminum garnet (YAl_5O_{12}, YAG) composites also display superior creep resistance than their single-phase counterparts [4,7,8] due to the mutual insolubility, high chemical stability and restrained grain growth of the alumina phase. Additionally, both fine-grained binary composites (grain sizes below about 1 μm) exhibit metal-like superplasticity at elevated temperatures [5,6,9,10], which contrasts strongly with the premature creep failure of monolithic alumina.

Among the multiphase alumina-based ceramics, directionally solidified Al_2O_3-based eutectic oxide composites, such as Al_2O_3/YAG, Al_2O_3/ZrO_2, $Al_2O_3/GdAlO_3$, Al_2O_3/YAG/ZrO_2, etc. have attracted much attention in the past because of their excellent thermo-mechanical behavior [11–18]; in particular, the ternary eutectic Al_2O_3/YAG/ZrO_2 system combines the high strength and creep resistance of the alumina and YAG phases with the superior fracture toughness of the zirconia phase. These properties derive directly from the singular lamellar microstructures developed during the solidification process, which improve the microstructural stability of the different phases. More recently, yttrium has been replaced by erbium in these eutectic oxides in order to be used as emitter in thermophotovoltaic generators [19–21]

* Corresponding author.
E-mail address: melendo@us.es (M. Jiménez-Melendo).

https://doi.org/10.1016/j.ceramint.2021.09.286
Received 29 June 2021; Received in revised form 19 August 2021; Accepted 9 September 2021
Available online 30 September 2021

while trying at the same time to preserve a high creep resistance. These devices operate at elevated temperatures converting thermal energy into narrowband near-infrared radiation, for which photovoltaic conversion is very efficient. Erbium is a promising candidate for such applications because of its strong thermally-excited emission band, which matches adequately the optical sensitive region of different photovoltaic cells [22–24].

The current techniques to produce directionally solidified eutectic ceramics do not cover however the requirements of the industry because they are costly and time consuming, and no suitable for mass production and components with custom sizes and shapes. Furthermore, their physical properties are very anisotropic, depending strongly on the solidification direction. These disadvantages can be reduced, at least partially, by using sintered particulate composites produced by conventional solid-state reaction routes. To our knowledge, only one study [25] has reported the fabrication and room-temperature mechanical properties of three-phase Al_2O_3/erbium aluminum garnet ($ErAl_5O_{12}$, EAG)/ZrO_2 sintered composites (hereinafter AEZ). The material was fabricated by hot pressing (1700 °C, 1 h), resulting fully dense samples (99.8% of relative density) with an average grain size of 4.7 μm. Notably, the authors reported a fracture toughness as high as 6.9 MPa $m^{1/2}$, even greater than the value of 4.5 MPa $m^{1/2}$ measured in the homologous directionally solidified eutectic composite with an interphase spacing (equivalent to the grain size in sintered composites) of 4.8 μm. The creep properties of these AEZ sintered composites are however still lacking, despite their relevance in the material selection and design of devices for high-temperature applications.

The aim of the present work was thus to evaluate the high-temperature plastic behavior of AEZ composites fabricated by a conventional solid-state reaction route of milling, calcining, and sintering of precursor powders. X-ray diffraction was used systematically to identify the crystalline phases and their volume fractions. The mechanical properties were evaluated by means of creep tests at constant load and at constant initial strain rate as a function of strain rate, temperature, and stress, and correlated with microstructural observations. The overall creep of the three-phase composite is compared to that of the single-phase counterparts in order to determine the rate-controlling phase.

2. Experimental procedure

2.1. Starting materials

Sintered Al_2O_3/EAG/ESZ composites with the eutectic composition were produced by a conventional solid-state reaction route. The starting high-purity commercial powders (99.99% purity, Sigma-Aldrich) were α-Al_2O_3, Er_2O_3 and monoclinic ZrO_2. Appropriate amounts of these powders (65.9 mol% Al_2O_3, 15.5 mol% Er_2O_3 and 18.6 mol% ZrO_2 [26]) were ball-milled in agate media for 1 h using a planetary ball mill. The resulting powder mixtures were calcined at different temperatures between 1200 and 1500 °C in air for 10 h and reground again to eliminate possible agglomerates. The particle size distribution of the different powder mixtures was analyzed by laser light scattering (Malvern Mastersizer 2000 with distilled water as carrier medium), resulting a number-based median particle size d_{50} of 1.14 μm for the as-received powder, 1.08 μm after the first milling step and 0.79 μm after calcination and second milling. TEM observations of the final powders showed that the average size particle was 0.7 ± 0.3 μm for the three phases, in agreement with the laser scattering measurements. X-ray structure analyses were systematically performed on the calcined powders in order to study the evolution of the different crystalline phases. Finally, the calcined mixtures were uniaxially pressed at 150 MPa into 20-mm diameter pellets and then isostatically cold pressed at 210 MPa. The resulting green pellets were sintered in air at 1500 °C for 10 h with low heating and cooling rates of 5 °C/min. The bulk density of the composites was determined from weight/dimensions measurements.

2.2. Structural and microstructural characterization

X-ray powder diffractograms were obtained using a Bruker D8 Advance A25 X-ray diffractometer with Cu K_α radiation and Ni filter, equipped with a scintillation detector in θ – 2θ Bragg-Brentano configuration (X-ray Laboratory, CITIUS, University of Sevilla, Spain). A continuous scan mode was used to collect 2θ data in the 10–120° range in steps of 0.015° and a scanning speed of 1.8°/min. Collected X-ray spectra were first processed by the Le Bail method followed by Rietveld refinement using the TOPAS 4.2 Bruker AXS software package to quantify the nature and amount of the different crystalline phases in the powders.

The microstructural characterization of as-fabricated and deformed composites was carried out using high-resolution scanning (HRSEM) and transmission (TEM) electron microscopy (Microscopy Service, CITIUS, University of Sevilla, Spain). In order to reveal the grain boundaries for SEM observations, sections were cut from the samples and mechanically polished using up to 0.25 μm-grade diamond paste, and then thermally etched at 1300 °C for 2 h in air. The relevant morphological parameters of the grains, size d (taken as the equivalent planar diameter), form factor F and preferential orientation angle θ, were measured by using a semiautomatic image analyzer. Thin films for TEM observations were obtained from the as-fabricated and deformed samples following a classical procedure of grinding and ion-thinning until electron transparency of sliced sections. Elemental composition analysis was performed by energy dispersive X-ray spectroscopy (EDS) in both SEM and TEM to characterize the various phases present in the composites.

2.3. Mechanical tests

Prismatic specimens of 5 × 3 × 3 mm in size were cut from the sintered pellets with a low-speed diamond saw and used for mechanical experiments. Compression tests were carried out in air at temperatures T between 1250 and 1450 °C. Two types of deformation experiments were performed: (i) under constant load in a creep machine, at nominal stresses between 50 and 120 MPa; the raw data, instantaneous specimen height vs. time, were plotted as $\log\dot{\varepsilon} - \varepsilon$ curves, where ε is the true stress and $\dot{\varepsilon} = d\varepsilon/dt$ is the instantaneous strain rate. And (ii) at constant crosshead speed in an universal testing machine at different initial strain rates $\dot{\varepsilon}_o$; the recorded data, load vs. time, were analyzed in σ - ε curves, where σ is the true stress.

The mechanical data were analyzed using the standard high-temperature power law for steady-state deformation [27]:

$$\dot{\varepsilon} = A\sigma^n d^{-p} \exp(-Q/RT) \quad (1)$$

where A is a parameter depending on the deformation mechanism, n is the stress exponent, p is the grain size exponent, Q is the activation energy for creep and R is the gas constant. The parameters n and Q, characteristics of the deformation mechanism, were measured from stress and temperature changes, respectively. The specimens were typically deformed to total strains of 50–60% (unless premature failure occurred) for subsequent microstructural observations.

3. Results and discussion

3.1. Phase evolution of the calcined powders

Fig. 1 depicts the XRD patterns of as-ground and 1200 °C- and 1400 °C-calcined powders. Only the three original phases, alumina, erbia and monoclinic zirconia were identified in the as-ground mixture, indicating that no additional phases formed during the milling process. The diffractogram is largely dominated by the erbia phase, in particular by the (222) reflections, due to the presence of Er cations. After calcination at 1200 °C, seven different phases were detected: the original

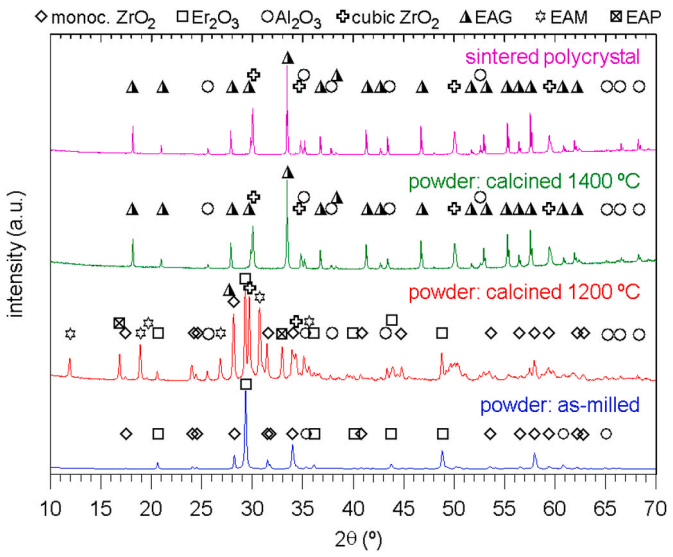

Fig. 1. X-ray diffraction patterns of Al_2O_3, Er_2O_3 and monoclinic ZrO_2 powder mixtures at various conditions: as-ground, after milling and calcination at 1200 and 1400 °C, and after sintering (powdered polycrystal). Bragg reflections were indexed according to the PDF-2002 reference patterns (International Centre for Diffraction Data, ICDD) as shown in the top of the figure.

precursor powders Al_2O_3, Er_2O_3, and monoclinic ZrO_2, as well as cubic zirconia and the three phases of the Al_2O_3/Er_2O_3 system: $Er_4Al_2O_9$ (EAM, monoclinic), $ErAlO_3$ (EAP, orthorhombic) and EAG (cubic). The different diffraction peaks were indexed according to the following PDF-2002 database reference patterns (International Centre for Diffraction Data, ICDD): α-Al_2O_3 (No. 05–0712), Er_2O_3 (No. 43–1007), monoclinic ZrO_2 (No. 36–0420), EAM (No. 32–0013), EAP (No. 24–0396), EAG (No. 32–0012) and erbia-stabilized cubic zirconia $Zr_{0.80}Er_{0.20}O_{1.90}$ (ESZ, No. 78–1307).

The intermediate phases EAM and EAP of the Al_2O_3/Er_2O_3 system gradually converted to cubic EAG with the calcination temperature, increasing the EAG content from 4.9 vol% at 1200 °C up to 27.4 vol% at 1300 °C and finally up to 39.9 vol% at 1400 °C and above. Similarly, monoclinic zirconia progressively transformed to cubic zirconia by alloying with the substitutional erbium cations provided by the Er_2O_3 phase. After calcination at 1400 °C, only the expected final phases α-Al_2O_3, EAG and cubic ZrO_2 were detected. In this case, the X-ray profile is dominated by the (420) peaks of the EAG phase (Fig. 1). Regarding the cubic zirconia phase, the $Zr_{0.80}Er_{0.20}O_{1.90}$ reference pattern provided the best match to the observed XRD profiles. After Rietveld refinement, a lattice parameter of a = 5.15449 ± 0.00003 Å was obtained for this phase, which corresponds (by using the Vegard's law with fitting parameters given by Yoshima et al. [28]) to an erbium content of 0.24 ± 0.02 at%, equivalent to 13.6 ± 2.2 mol% E_2O_3 fully-stabilized cubic zirconia. This erbia molar content is intermediate between those reported in directionally solidified AEZ eutectics grown from the melt by different techniques: 11.1 [17], 12.5 [26], 15.0 [14], 15.2 [18] and 15.3 mol% E_2O_3 [12].

The experimental volume fractions of Al_2O_3, EAG and 13.6 mol% Er_2O_3-cubic stabilized ZrO_2 (ESZ) phases estimated from XRD spectra are 39.2 ± 0.3%, 39.9 ± 0.3% and 20.9 ± 0.2%, respectively. These fractions are consistent with the values reported in melt-grown AEZ eutectics by Mesa et al. [14] (39 ± 1%, 40 ± 1% and 21 ± 1%) and by Wang and Liu [16] (38.2 ± 1.9%, 44.1 ± 2.3% and 17.7 ± 2.2%), as well as with the theoretical values calculated using the eutectic composition (42.0%, 39.7% and 18.3%). No further evolution of the crystallographic phases and volume fractions was observed with the sintering process (Fig. 1).

3.2. Microstructural characterization of sintered composites

Fig. 2 depicts representative micrographs of the grain structure of the as-sintered polycrystals. Fig. 2(a) is a secondary electron SEM image overlaid with its EDS composition map of a polished and thermally-etched sample cross-section showing the three phases (which are hardly distinguished from each other by SEM alone). The microstructure is formed by a homogeneous distribution of equiaxed grains, with little porosity mainly located at triple grain junctions. TEM observations indicated that the grain boundaries are well facetted, equiaxed and free of secondary grain boundary phases (Fig. 2(b) and (c)). No dislocations were observed in the grains except for occasional dislocation arrays in the larger alumina grains (Fig. 2(c)), which are likely due to the residual stresses generated during the sintering and cooling processes by the mismatch in thermal expansion coefficients between the alumina and the other two phases, particularly zirconia [14].

The average bulk density of the sintered composites was 5420 ± 50 kg/m^3. The theoretical density, calculated from the expected phase composition, is 5500 kg/m^3 (densities of 3990, 6380 and 6770 kg/m^3 have been used for alumina, EAG and 13.6 mol% Er_2O_3-cubic stabilized zirconia, respectively), resulting a relative density of nearly 99%. To our knowledge, only one study has reported the fabrication of AEZ polycrystals [25]. In that work, the composites were fabricated with the eutectic composition directly from the original precursor powders (alumina, erbia and zirconia) without previous calcination by hot-pressing at 1700 °C, obtaining a relative density of 99.8% and an average grain size of 4.7 μm. We have also tried to fabricate the AEZ composites from the non-calcined raw powders; though the observed crystalline phases Al_2O_3, EAG and ESZ and their respective volume fractions were identical to those found in the composite fabricated from calcined powders, the relative density was as low as 60%, with grain sizes of 0.5 μm for the three phases (Fig. 2(d)).

The grain size distribution of the three phases in the composite is shown in Fig. 3, which follow a log-normal law as usually found in ceramic materials. Zirconia has the smaller grain size, with an average value d = 0.9 ± 0.5 μm (uncertainty indicates the standard deviation of the grain size distribution). The other two phases Al_2O_3 and EAG show the same grain size distributions, with mean values d = 1.1 ± 0.5 μm and d = 1.1 ± 0.6 μm, respectively. These values are practically identical to those found in a three-phase alumina/YAG/yttria-stabilized cubic zirconia (YSZ) sintered composite with the eutectic composition fabricated by a similar processing route (d = 1.1, 1.0 and 0.8 μm for Al_2O_3, YAG and YSZ phases, respectively) [29]. The average form factor of the grains is F = 0.8 ± 0.1 for the three phases, indicating a regular grain growth during sintering, without preferential grain orientation. Although pristine alumina is prone to exaggerated grain coarsening, it has a restricted grain growth in the presence of dopants (such as zirconium and rare earths [30–34]) or second particulate phases (such as in Al_2O_3/ZrO_2 [5,6,35,36], Al_2O_3/YAG [37] and ternary alumina-based composites [29,38–40]). For instance, it has been reported in Al_2O_3/YAG composites [37] that the grain size of undoped alumina sintered at 1400 °C decreased from several μm down to below 1 μm when alloyed with 30 vol% YAG sintered at 1600 °C, both phases having similar grain sizes.

3.3. High-temperature plastic deformation of AEZ composites

Fig. 4 shows typical curves of the variation of the true stress σ with true strain ε for AEZ composites deformed at temperatures between 1300 and 1450 °C in air at an initial strain rate $\dot{\varepsilon}_o = 2 \times 10^{-5}$ s^{-1} (solid lines). The compound displays a progressive transition from brittle-to-ductile regime with increasing temperature. At 1300 °C, the composite failed after reaching a maximum stress of 450 MPa, with little plastic deformation. At 1350 °C, the composite exhibits a semiductile behavior characterized by a continuous decrease of stress with strain after the yield point (flow softening), indicating a progressive degradation of the material by creep damage; despite the softening, no signs of macroscopic

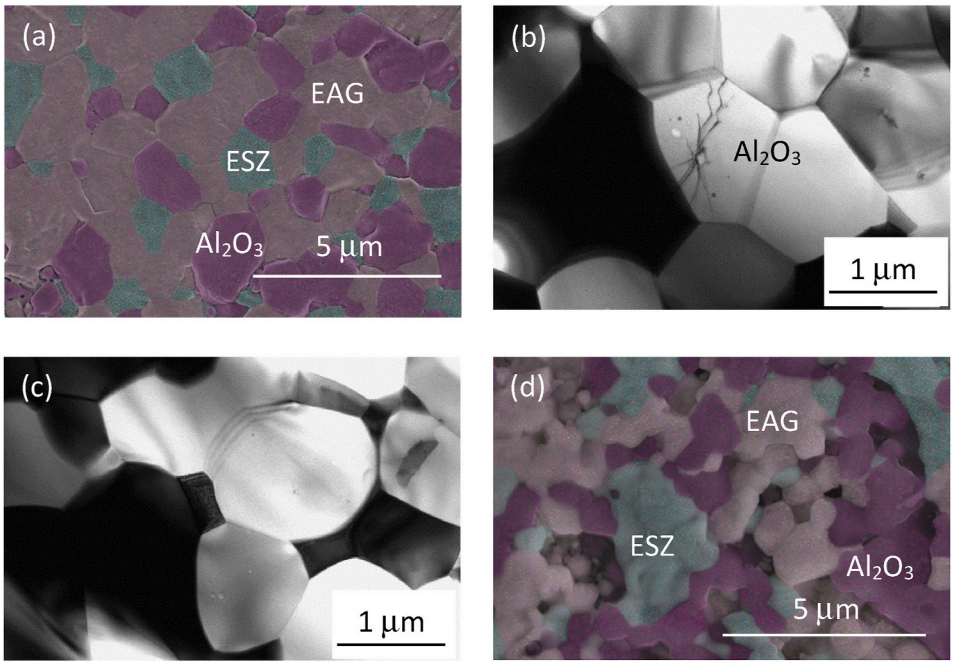

Fig. 2. Microstructure of eutectic-composition Al_2O_3/EAG/ZrO_2 sintered composites: (a) SEM image/EDS composition map showing the three phases: Al_2O_3, EAG and cubic ZrO_2 (ESZ); (b) and (c) TEM micrographs of the grain structure, showing occasional dislocation arrays in the larger alumina grains; (d) SEM image/EDS composition map of a porous composite obtained directly from the precursor powders without previous calcination.

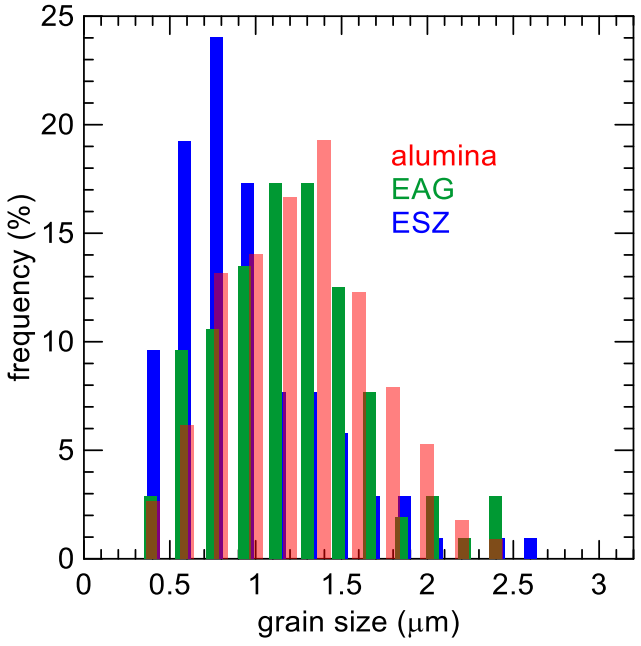

Fig. 3. Grain size distributions of the Al_2O_3, EAG and erbia fully-stabilized cubic ZrO_2 (ESZ) phases in the eutectic-composition AEZ sintered composites.

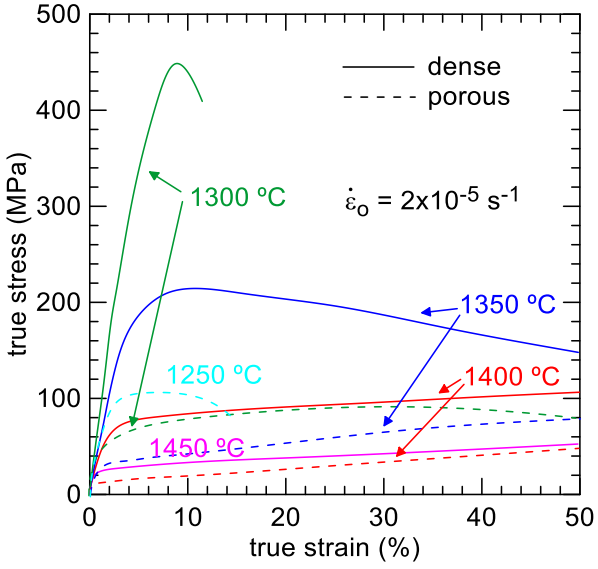

Fig. 4. Variation of the true stress σ with true strain ε for AEZ sintered composites (solid lines) as a function of the temperature obtained at an initial strain rate of $\dot{\varepsilon}_o = 2 \times 10^{-5}$ s^{-1}. Curves for the porous composite (60% relative density) obtained directly from non-calcined precursor powders are also shown (dashed lines).

failure were found even after true strains of 50%. Finally, at temperatures of 1400 °C and above, extended steady states of deformation (secondary creep regime) were attained. In this ductile regime, the slope of the σ – ε curves is slightly positive because of the continuous shortening of the sample during compression.

Fig. 4 also shows the σ – ε curves obtained at different temperatures of the porous (60% density) AEZ composites fabricated directly from non-calcined precursor powders (dashed lines). A brittle-to-ductile transition with increasing temperature was also found, but shifted down to about 100 °C with respect to the dense polycrystals, owing to their much higher porosity and smaller grain size. Regarding the flow stresses in steady state, the porous composite is about 7 times softer than the dense material (Fig. 4).

With regard to the microstructure of the deformed composites, no appreciable changes in shape, size and preferential orientation of the grains relative to the unstrained state were observed in the ductile region, despite the large strains attained (Fig. 5(a)). Consequently, the grains had to slide on each other along their boundaries to accommodate the macroscopic strain without deformation of the grain themselves. Such a deformation mechanism of grain boundary sliding has been

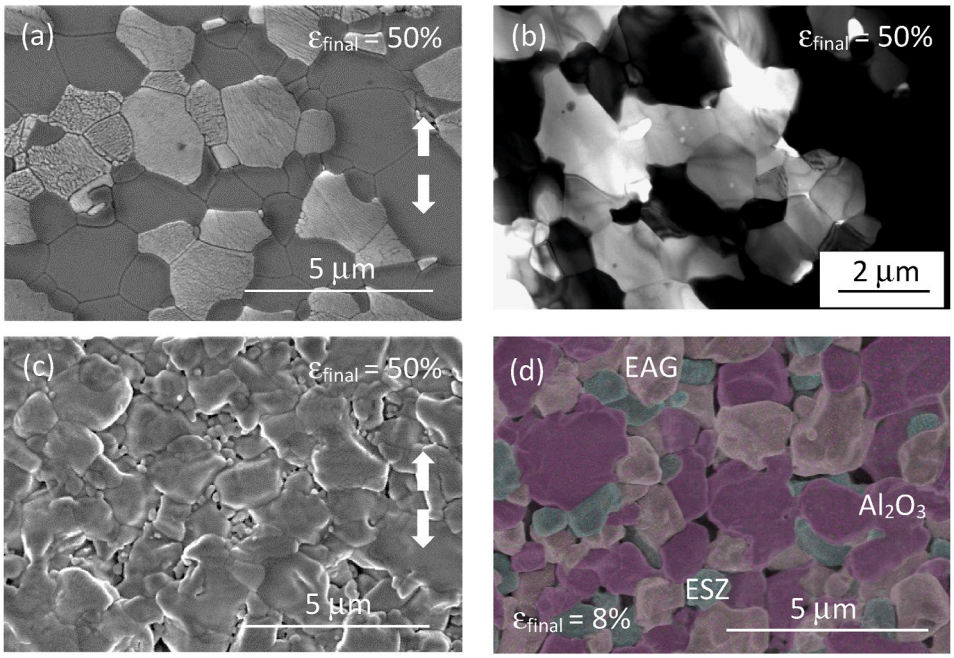

Fig. 5. Microstructure of deformation of AEZ sintered composites: (a) SEM (polished surface) and (b) TEM images of a specimen 50%-strained in the ductile region, 1450 °C; (c) SEM image (polished surface) of a specimen 50%-strained in the semibrittle region, 1350 °C; and (d) SEM image/EDS composition map (fracture surface) of a specimen failed at 8% strain, 1300 °C. Arrows in (a) and (c) indicate the load direction.

widely reported in the creep of fine-grained metals and ceramics [5,6,9,41–44]. TEM observations of specimens 50%-deformed in steady-state conditions (Fig. 5(b)) confirmed the absence of microstructural evolution during testing: the grains remain equiaxed without signs of cavitation along the grain boundaries, with occasional dislocation arrays only in the larger alumina grains. It can be thus concluded that dislocations do not play any significant role in the secondary creep regime of AEZ composites.

As long as the deformation conditions become more severe (lower temperatures and higher strain rates), the local stresses generated during the sliding of the grains cannot be fully accommodated and cavities appear at grain boundaries, as shown in Fig. 5(c) for a specimen 50%-deformed in the semibrittle region. These microcavities, however, did not coalesce into cracks despite the large strains attained, resulting in a flaw-tolerant regime. TEM observations of specimens 50%-deformed in this semibrittle regime have shown that the grains are more stressed than in the ductile region but still free of dislocations. Finally, at the worst testing conditions, the microcavities coalesce into microcracks leading to the fracture of the material. SEM observations of these fracture surfaces (Fig. 5(d)) show that the fracture mode was mainly intragranular in the alumina phase and intergranular in the zirconia and garnet phases. Although the fracture mode of pristine alumina is intergranular [45], it changes to intragranular fracture upon the addition of impurities/dopants which segregate strongly to the grain boundaries [30,46,47]. Such an effect is very likely to occur in the present composites due to the unintentional doping of the alumina phase by the zirconium and erbium cations of the ESZ and EAG phases (this point is discussed further in Section 3.6).

3.4. Power-law creep parameters n and Q

Creep tests at constant load have been performed in steady state to determine the stress exponent n and the activation energy Q of the power-law creep equation (Eq. (1)), which characterize the deformation mechanism [9,27]. Fig. 6(a) shows a representative $\log \dot{\varepsilon} - \varepsilon$ curve obtained at 1400 °C with several determinations of n by up- and down-load changes (differential method) between 100 and 120 MPa.

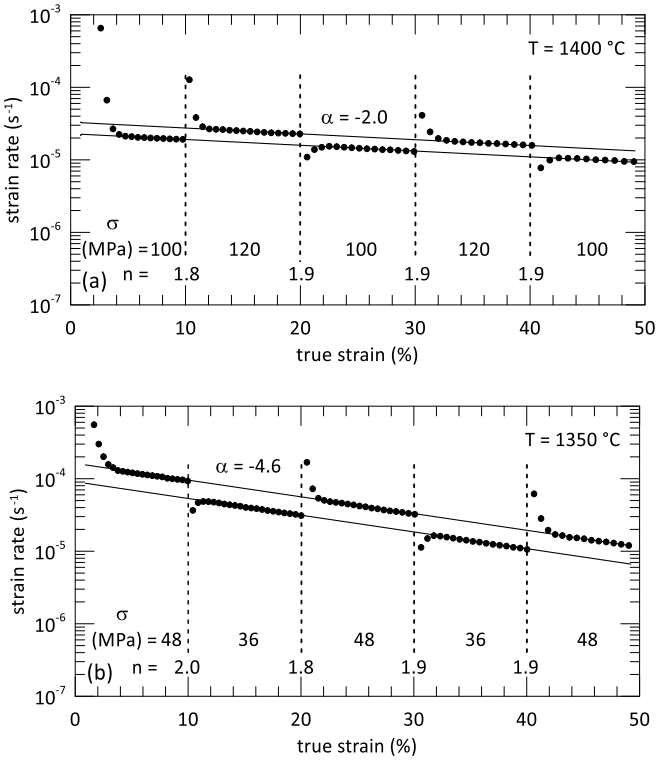

Fig. 6. Creep curves plotted as $\log \dot{\varepsilon} - \varepsilon$ for (a) dense and (b) porous AEZ composites deformed in steady-state conditions. Several determinations of the stress exponent n (Eq. (1)) by up- and down-load changes are shown.

The steady states are characterized by a constant negative slope of the $\log \dot{\varepsilon} - \varepsilon$ curve because of the increase in specimen section during compression at constant load. A mean value of $n = 1.9 \pm 0.1$ was estimated, very close to the value of 2 reported for superplastic materials where grain boundary sliding is the dominant mechanism of

deformation [6,9,31,41–43,48]. For homogeneous deformation (i.e., neither sample buckling, cavitation, grain coarsening or other flaws occur during testing), the slope α of the $\log \dot{\varepsilon} - \varepsilon$ curve is equal to -n; as shown Fig. 6(a), an experimental slope $\alpha = -2.0$ was found, in excellent agreement with the value of n measured by stress changes. Additionally, the strain rate levels are maintained after up- and down-load changes, indicating the absence of microstructural changes during creep, in agreement with SEM and TEM observations. Furthermore, the different stages of the $\log \dot{\varepsilon} - \varepsilon$ curves display very short transients before attaining the steady state (within a strain <2%) upon up- and down-stress changes (Fig. 6(a)), suggesting again that a dislocation-driven mechanism, which needs the establishment of a dislocation substructure prior to the attainment of the steady state, does not participate in the plastic flow of the composites.

A stress exponent n close to 2 has been systematically reported in the creep of fine-grained metals and ceramics where grain boundary sliding is the main deformation mechanism [6,9,31,41–43,48]. Such a value is also predicted by most theoretical and semiphenomenological models developed to explain the superplastic behavior of fine-grained materials [9]. The set of experimental results found in the ductile regime: stress exponent close to 2, extended steady states of deformation, absence of changes in grain size and morphology after large strains, as well as the absence of dislocation activity and creep transients, supports the conclusion that the creep of AEZ sintered composites takes place by grain boundary sliding.

Several tests at constant load were conducted on the porous composites (60% density). Fig. 6(b) shows a typical creep curve obtained at 1350 °C with several determinations of n by load changes. Again, a stress exponent of nearly 2 was found; in this material, however, the $\log \dot{\varepsilon} - \varepsilon$ curves exhibit a slope $|\alpha| > n$, due to the progressive densification of the samples during testing.

When deformation is achieved by grain boundary sliding, the steady-state flow rate is usually controlled by the diffusion necessary to accommodate the local stresses generated during the sliding of the grains [9,27]. Then, the creep activation energy Q (Eq. (1)) can be identified with the diffusion energy of the slowest moving species in the compound along the faster path. In the present study, Q was measured by up- and down-temperature changes of 50 °C in steady-state conditions, as illustrated in Fig. 7 for a specimen deformed at a fixed initial stress of 100 MPa with temperature jumps between 1400 and 1450 °C. An average value of $Q = 700 \pm 60$ kJ/mol was found, which is practically the same value of $Q = 680 \pm 60$ kJ/mol reported for a three-phase AYZ sintered composite with similar microstructure [29]. Again, the maintenance of the strain rate levels after positive and negative temperature jumps indicates that no significant microstructural evolution took place during testing, with experimental slopes |α| of about 2 (Fig. 7). The measured Q value of 700 kJ/mol is discussed in the following Section in relation to the creep and diffusion energies of the monolithic constituents of the AEZ composite.

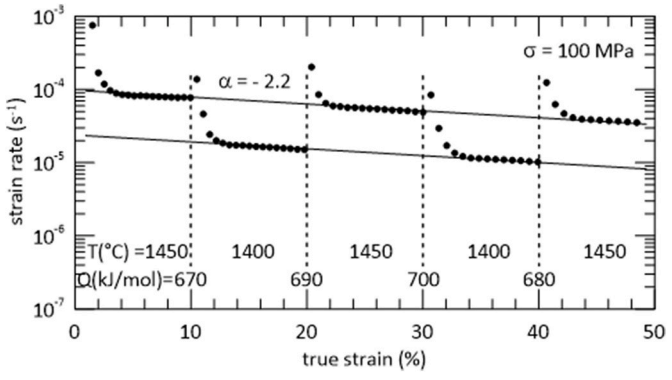

Fig. 7. Creep curve $\log \dot{\varepsilon} - \varepsilon$ for dense AEZ composite deformed in steady-state conditions. Several determinations of the creep activation energy Q (Equation (1)) by up- and down-temperature changes are shown.

3.5. Creep-controlling phase in AEZ composites

The variation of strain rate with stress at 1400 °C of the AEZ sintered composite is shown in Fig. 8 (black solid line). In order to determine the rate-controlling phase, this overall creep rate should be compared to that of the monolithic constituent phases. Unfortunately, there are not enough data available in the literature for such a comparison. The diffusion and creep behavior of alumina have been widely reported [4,10,31–33,48–50], but there are no data for EAG and ESZ monoliths. Therefore, the comparison with the isostructural oxides yttria fully-stabilized cubic zirconia (YSZ) and yttrium aluminum garnet (YAG), where Er^{3+} is replaced by Y^{3+} (ionic radii $Er^{3+}_{VIII} = 1.004$ Å and $Y^{3+}_{VIII} = 1.019$ Å), seems to be pertinent in this context; such a comparison is supported by the similarity of creep rates exhibited by the present composite and a three-phase AYZ sintered composite with d = 1 μm deformed in the same experimental conditions, which differ only by a factor of 2 [29].

Fig. 8 displays the normalized strain rates for undoped monolithic alumina [4,31], YSZ [4,51] and YAG [4,52] at 1400 °C and 1 μm; data have been compensate with the values of Q given by the respective authors and a grain size exponent of p = 2 (the most reported value, and intermediate between the values of 1–3 found for grain boundary sliding [6,8,9,31,41,48]) in Eq. (1). Despite the scatter in the reported data, which is not uncommon in the creep literature, it can be seen that the creep rate of the AEZ composite is about one order of magnitude lower than those of the single-phase monoliths. This apparently contradictory finding can be also observed in the creep of binary alumina/EAG composites [11] (black slashed line in Fig. 8).

Such unexpected behavior can be explained on the basis of the enhanced creep resistance exhibited by cation-doped fine-grained alumina relative to the undoped material. It has been shown that the addition of trace amounts (≤1000 ppm) of selected dopants such as

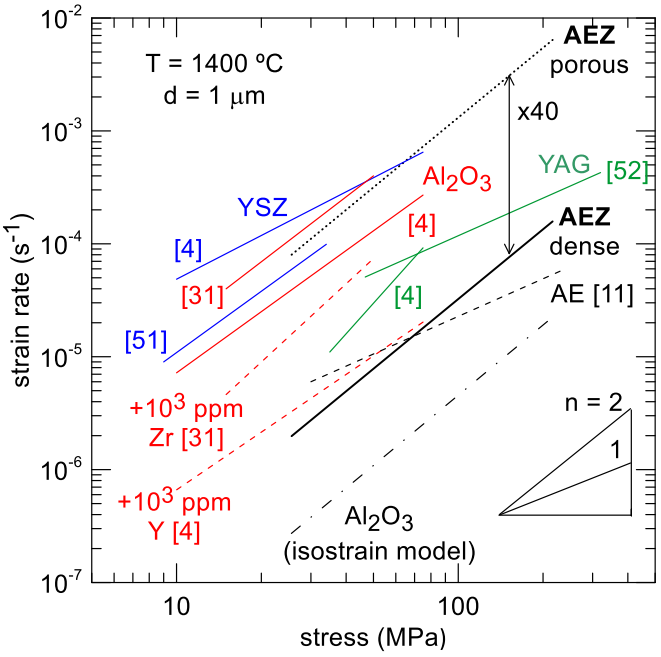

Fig. 8. Variation of strain rate with stress at T = 1400 °C and d = 1 μm for dense and porous AEZ composites. Creep data for monolithic YSZ, YAG, and undoped and Zr- and Y-doped alumina, and for a duplex Al_2O_3/EAG sintered composite (AE), are also shown. Prediction of the isostrain model for the alumina phase in the AEZ composite is included (black dot -dashed line).

yttrium, lanthanum, neodymium or zirconium reduces the creep rate by 1–3 orders of magnitude [4,31,32,34,48] (red slashed lines in Fig. 8). The decrease is even more effective when doubly doped with specific pairs of cations such as Y/Zr or Nd/Zr; for example, Yasuda et al. [32] reported reductions by factors of 25 and 100 when singly doped with Zr and Y, respectively, and by a factor of 400 when doubly doped with Y/Zr.

Furthermore, the creep hardening of doped alumina was systematically accompanied by a significant increase in activation energy with respect to undoped alumina. As shown in Fig. 9, the creep energy (red slashed areas) raises from Q = 410–520 kJ/mol in nominally pure alumina up to 670–760 kJ/mol in Zr-doped alumina [31,48] and up to 700–820 kJ/mol in Y-doped alumina [4,48,53]. Diffusion measurements in alumina show the same trend: doping with yttrium decreases the diffusivity of oxygen (which seems to be the slower ion, though it is still a matter of debate due to the highly extrinsic character of the alumina) at grain boundaries by 2–3 orders of magnitude, increasing at the same time the oxygen self-diffusion energy (red solid areas in Fig. 9) [49,50,54]. These results were attributed to the segregation of dopant cations along the alumina grain boundaries, which blocked critical diffusion paths and consequently lowered the strain rates.

Assuming that erbium replaces yttrium in the present ternary composite without significant changes, the previous results suggest that alumina is the more creep-resistant phase in the AEZ composite because of the presence of erbium and zirconium cations along the alumina grain boundaries, which most likely occurred during the powder calcination and sintering steps. The high creep energy of 700 kJ/mol found in the present AEZ composite, similar to that reported in binary alumina/YAG [4,52], alumina/YSZ [4] and alumina/EAG [11] composites (AY, AZ, and AE, respectively, in Fig. 9), compares well with the Q values measured in Y^{3+}- and Zr^{4+}-doped monolithic alumina, supporting this idea. In such conditions, the overall creep behavior of the composite can be modelled by the isostrain condition, i.e., the more creep-resistant phase controls the composite strain rate [4,7,10]. According to the model, the alumina phase (with a volume fraction f = 39.2% in the ternary composite) would exhibit a creep rate lower than that of the composite by a factor of $(1/f)^2 = 6.5$ (black dot-dashed line in Fig. 8), which corresponds to a reduction of more than two orders of magnitude relative to the average behavior of undoped alumina (Fig. 8). This result is in close agreement with the hardening noted above for yttrium- and zirconium-doped alumina.

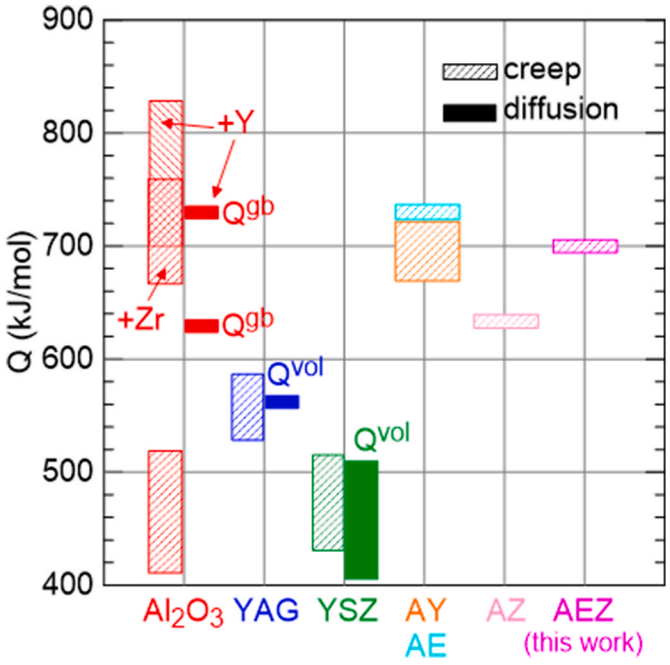

Fig. 9. Creep activation energies for steady-state flow (dashed areas) in monolithic alumina, YAG and YSZ, as well as in binary alumina/YSZ (AZ), alumina/YAG (AY) and alumina/EAG (AE) sintered composites, and in the present three-phase AEZ composite. Self-diffusion energies of the slower moving species in alumina (oxygen), YAG and YSZ (cations) are also shown (solid areas); Q^{gb} = grain boundaries, Q^{vol} = volume.

Waku et al. [11] reported the compressive creep at 1600 °C of an eutectic-composition binary Al_2O_3/EAG sintered composite (AE) fabricated by hot-pressing at 1700 °C for 1 h in vacuum, with an average grain size of d = 4 μm. Using the value of Q = 730 kJ/mol measured by the authors in AE composites grown from the melt and p = 2 in Eq. (1), the normalized strain rate is shown in Fig. 8 (black dashed line). It overlaps correctly onto the present composite, but with a different stress dependence: n = 2 in the ternary composite with d = 1 μm and n = 1 in the binary composite with d = 4 μm. Such a decrease of n when increasing grain size above about 1 μm has been reported previously in different metallic and ceramic materials, and its origin is still a matter of debate [41,44,55,56]. The comparison of the strain rates and creep energies in AE and AEZ composites suggests than the same phase controls the creep behavior in both materials.

On the other hand, the creep behavior of the porous composite (60% density) can be analyzed by the stress-porosity model based on the minimum solid area (MSA) proposed by Rice [57] to describe the mechanical properties of porous materials. Assuming a simple model of cubic stacking of spherical pores, the applied stress σ_P in the composite with porosity P is related to the actual stress acting on the ceramic phases σ by [57].

$$\frac{\sigma_P}{\sigma} = 1 - \frac{\pi}{4}\left(\frac{6P}{\pi}\right)^{2/3} \quad (2)$$

With P = 0.40, Eq. (2) predicts $\sigma \simeq 3\sigma_P$, corresponding to a strain rate of $3^n = 9$ (n = 2) times higher than the dense material. When the difference in grain size is considered (d = 0.5 and 1.0 μm in the porous and dense composites, respectively), the difference increases up to $9x(1.0/0.5)^p = 36$ (p = 2), in fairly good agreement with the experimental data (Fig. 8). In this regard, Owen and Chokshi [58] demonstrated that the deformation mechanisms in porous (densities of 60%–77%) and fully dense yttria-stabilized tetragonal zirconia polycrystals were identical, which seems to be also the case in the present materials.

4. Conclusions

$Al_2O_3/Er_3Al_5O_{12}$ (EAG)/erbium fully-stabilized cubic ZrO_2 (ESZ) sintered composites with the ternary eutectic composition have been successfully fabricated by a conventional solid-state reaction route, starting with high-purity commercial powders of Al_2O_3, Er_2O_3 and monoclinic ZrO_2 zirconia. The final phases Al_2O_3, EAG and ESZ, without other intermediate phases, were obtained after calcination at 1400 °C. Bulk composites with a relative density of 98.5% were obtained by sintering at 1500 °C in air for 10 h. The microstructure is formed by a homogeneous distribution of equiaxed grains with average sizes of 1 μm for the three phases. Compressive mechanical tests were performed at constant cross-head speed and at constant load in air at high temperatures. A transition brittle-to-ductile was found with increasing temperature. Extended steady states of deformation were attained in the ductile region, characterized by a stress exponent n of 2 and without noticeable changes in grain morphology and dislocation activity relative to the unstrained state, indicating that grain boundary sliding is the primary deformation mechanism. As the temperature decreases, a gradual transition towards a brittle behavior was found, with cavity formation along grain boundaries and final sample failure. The comparison with the single-phase constituents suggests that alumina is the rate-controlling phase in the composite because of the presence of erbium and zirconium cations provided by the other two phases, which significantly increases both the creep resistance and the creep energy of the alumina

phase, as found in yttrium- and zirconium-doped monolithic alumina. It is shown that yttrium can be replaced by erbium in three-phase alumina/aluminum garnet/cubic zirconia sintered polycrystals without detriment of the high-temperature creep properties. The combination of high plasticity and creep resistance exhibited by the AEZ sintered composite suggests that it can be tailored to compete with melt-grown eutectic analogs.

Declaration of competing interest

The authors declare that they have no known competing financial interests or personal relationships that could have appeared to influence the work reported in this paper.

Acknowledgment

This work was supported by the Project no. MAT2009-13979-C03-01, Ministerio de Ciencia e Innovación, Spain.

References

[1] D.S. Wilkinson, C.H. Caceres, A.G. Robertson, Damage and fracture mechanisms during high-temperature creep in hot-pressed alumina, J. Am. Ceram. Soc. 74 (1991) 922–933, https://doi.org/10.1111/j.1151-2916.1991.tb04323.x.
[2] B.J. Dalgleish, E.B. Slamovich, A.G. Evans, Duality in the creep rupture of a polycrystalline alumina, J. Am. Ceram. Soc. 68 (1985) 575–581, https://doi.org/10.1111/j.1151-2916.1985.tb16158.x.
[3] J.D. French, H.M. Chan, M.P. Harmer, G.A. Miller, High-temperature fracture toughness of duplex microstructures, J. Am. Ceram. Soc. 79 (1996) 58–64, https://doi.org/10.1111/j.1151-2916.1996.tb07880.x.
[4] J.D. French, J. Zhao, M.P. Harmer, H.M. Chan, G.A. Miller, Creep of duplex microstructures, J. Am. Ceram. Soc. 77 (1994) 2857–2865, https://doi.org/10.1111/j.1151-2916.1994.tb04515.x.
[5] D.M. Owen, A.H. Chokshi, The constant stress tensile creep behaviour of a superplastic zirconia-alumina composite, J. Mater. Sci. 29 (1994) 5467–5474, https://doi.org/10.1007/BF01171563.
[6] L. Clarisse, R. Baddi, A. Bataille, J. Crampon, R. Duclos, J. Vicens, Superplastic deformation mechanisms during creep of alumina-zirconia composites, Acta Mater. 45 (1997) 3843–3853, https://doi.org/10.1016/S1359-6454(97)89771-6.
[7] H. Duong, J. Wolfenstine, Creep behavior of fine-grained two-phase Al2O3Y3Al5O12 materials, Mater. Sci. Eng. A 172 (1993) 173–179, https://doi.org/10.1016/0921-5093(93)90438-K.
[8] L.N. Satapathy, A.H. Chokshi, Microstructural development and creep deformation in an alumina-5% yttrium aluminum garnet composite, J. Am. Ceram. Soc. 88 (2005) 2848–2854, https://doi.org/10.1111/j.1551-2916.2005.00307.x.
[9] T.G. Nieh, J. Wadsworth, O.D. Sherby, Superplasticity in Metals and Ceramics, Cambridge University Press, 1997, https://doi.org/10.1017/CBO9780511525230.
[10] A. Morales-Rodríguez, A. Domínguez-Rodríguez, G. de Portu, M. Jiménez-Melendo, Creep mechanisms of laminated alumina/zirconia-toughened alumina composites, J. Eur. Ceram. Soc. 29 (2009) 1625–1630, https://doi.org/10.1016/j.jeurceramsoc.2008.09.017.
[11] Y. Waku, N. Nakagawa, H. Ohtsubo, A. Mitani, K. Shimizu, Fracture and deformation behaviour of melt growth composites at very high temperatures, J. Mater. Sci. 36 (2001) 1585–1594, https://doi.org/10.1023/A:1017519113164.
[12] L. Mazerolles, N. Piquet, M.F. Trichet, L. Perrière, D. Boivin, M. Parlier, New microstructures in ceramic materials from the melt for high temperature applications, Aero. Sci. Technol. 12 (2008) 499–505, https://doi.org/10.1016/j.ast.2007.12.002.
[13] F.A. Huamán-Mamani, M. Jiménez-Melendo, M.C. Mesa, P.B. Oliete, Microstructure and high-temperature mechanical behavior of melt-growth Al 2O 3/Er 3Al 5O 12/ZrO 2 ternary eutectic composites, in: J. Alloys Compd, Elsevier, 2012, pp. S527–S531, https://doi.org/10.1016/j.jallcom.2012.01.105.
[14] M.C. Mesa, P.B. Oliete, Á. Larrea, V.M. Orera, Directionally solidified Al 2 O 3- Er 3 Al 5 O 12- ZrO 2 eutectic ceramics with interpenetrating or nanofibrillar microstructure: residual stress analysis, J. Am. Ceram. Soc. 95 (2012) 1138–1146, https://doi.org/10.1111/j.1551-2916.2011.05068.x.
[15] J.I. Peña, M. Larsson, R.I. Merino, I. de Francisco, V.M. Orera, J. LLorca, J. Y. Pastor, A. Martín, J. Segurado, Processing, microstructure and mechanical properties of directionally-solidified Al2O3-Y3Al5O12-ZrO2 ternary eutectics, J. Eur. Ceram. Soc. 26 (2006) 3113–3121, https://doi.org/10.1016/j.jeurceramsoc.2005.11.005.
[16] S. Wang, J. Liu, Microstructure and growth characteristics of Al2O3/Er2O3/ZrO2 solidified ceramics with different compositions, J. Eur. Ceram. Soc. 41 (2021) 4284–4293, https://doi.org/10.1016/j.jeurceramsoc.2021.01.058.
[17] Y. Waku, S. Sakata, A. Mitani, K. Shimzu, A. Ohtsuka, M. Hasebe, Microstructure and high-temperature strength of Al2O 3/Er3Al5O12/ZrO2 ternary melt growth composite, J. Mater. Sci. 40 (2005) 711–717, https://doi.org/10.1007/s10853-005-6311-z.
[18] S. Wang, J. Liu, S. Zhai, Microstructure and mechanical properties of Al 2 O 3/Er 3 Al 5 O 12/ZrO 2 prepared by a high-frequency zone melting method, Int. J. Refract. Metals Hard Mater. 81 (2019) 291–298, https://doi.org/10.1016/j.ijrmhm.2019.03.011.
[19] N. Nakagawa, H. Ohtsubo, Y. Waku, H. Yugami, Thermal emission properties of Al2O3/Er3 Al5O12 eutectic ceramics, J. Eur. Ceram. Soc. 25 (2005) 1285–1291, https://doi.org/10.1016/j.jeurceramsoc.2005.01.031.
[20] M.C. Mesa, P.B. Oliete, R.I. Merino, V.M. Orera, Optical absorption and selective thermal emission in directionally solidified Al2O3-Er3Al5O12 and Al2O3-Er3Al5O12-Z rO2 eutectics, J. Eur. Ceram. Soc. 33 (2013) 2587–2596, https://doi.org/10.1016/j.jeurceramsoc.2013.05.001.
[21] P.B. Oliete, A. Orera, M.L. Sanjuán, R.I. Merino, Selective thermal emission of directionally solidified Al2O3/Y3−xErxAl5O12 eutectics: influence of the microstructure, temperature and erbium content, Sol. Energy Mater. Sol. Cells 174 (2018) 460–468, https://doi.org/10.1016/j.solmat.2017.09.031.
[22] B. Bitnar, W. Durisch, J.C. Mayor, H. Sigg, H.R. Tschudi, Characterisation of rare earth selective emitters for thermophotovoltaic applications, Sol. Energy Mater. Sol. Cells 73 (2002) 221–234, https://doi.org/10.1016/S0927-0248(01)00127-1.
[23] D. Diso, A. Licciulli, A. Bianco, M. Lomascolo, G. Leo, M. Mazzer, S. Tundo, G. Torsello, A. Maffezzoli, Erbium containing ceramic emitters for thermophotovoltaic energy conversion, Mater. Sci. Eng. B Solid-State Mater. Adv. Technol 98 (2003) 144–149, https://doi.org/10.1016/S0921-5107(03)00036-9.
[24] A. Licciulli, D. Diso, G. Torsello, S. Tundo, A. Maffezzoli, M. Lomascolo, M. Mazzer, The challenge of high-performance selective emitters for thermophotovoltaic applications, Semicond. Sci. Technol. 18 (2003) 174, https://doi.org/10.1088/0268-1242/18/5/306.
[25] S. Wang, J. Liu, Comparison of Al2O3/Er3Al5O12/ZrO2 ceramics with eutectic composition prepared using hot-pressing sintering and melt growing, Mater. Sci. Eng. A 774 (2020), https://doi.org/10.1016/j.msea.2020.138932.
[26] S.M. Lakiza, L.M. Lopato, Phase diagram of the Al2O3-ZrO2-Er2O3 system, J. Eur. Ceram. Soc. 28 (2008) 2389–2397, https://doi.org/10.1016/j.jeurceramsoc.2008.01.012.
[27] J.-P. Poirier, Creep of Crystals, Cambridge University Press, 1985, https://doi.org/10.1017/CBO9780511564451.
[28] M. Yashima, N. Ishizawa, M. Yoshimura, Application of an ion-packing model based on defect clusters to zirconia solid solutions: II, applicability of Vegard's law, J. Am. Ceram. Soc. 75 (1992) 1550–1557, https://doi.org/10.1111/j.1151-2916.1992.tb04223.x.
[29] F.A. Huamán-Mamani, C. Jiménez-Holgado, M. Jiménez-Melendo, Fabrication and creep properties of eutectic-composition Al2O3/YAG/YSZ sintered composites, J. Eur. Ceram. Soc. (2021), https://doi.org/10.1016/J.JEURCERAMSOC.2021.07.055.
[30] G.D. West, J.M. Perkins, M.H. Lewis, The effect of rare earth dopants on grain boundary cohesion in alumina, J. Eur. Ceram. Soc. 27 (2007) 1913–1918, https://doi.org/10.1016/j.jeurceramsoc.2006.07.001.
[31] F. Wakai, T. Nagano, T. Iga, Hardening in creep of alumina by zirconium segregation at the grain boundary, J. Am. Ceram. Soc. 80 (1997) 2361–2366, https://doi.org/10.1111/j.1151-2916.1997.tb03128.x.
[32] S. Yasuda, H. Yoshida, T. Yamamoto, T. Sakuma, Improvement of high-temperature creep resistance in polycrystalline Al_2O_3 by cations Co-doping, Mater. Trans. 45 (2004) 2078–2082, https://doi.org/10.2320/matertrans.45.2078.
[33] L.A. Xue, X. Wu, I.-W. Chen, Superplastic alumina ceramics with grain growth inhibitors, J. Am. Ceram. Soc. 74 (1991) 842–845, https://doi.org/10.1111/j.1151-2916.1991.tb06935.x.
[34] Y.Z. Li, C. Wang, H.M. Chan, J.M. Rickman, M.P. Harmer, J.M. Chabala, K. L. Gavrilov, R. Levi-Setti, Codoping of alumina to enhance creep resistance, J. Am. Ceram. Soc. 82 (1999) 1497–1504, https://doi.org/10.1111/j.1151-2916.1999.tb01947.x.
[35] F. Wakai, H. Kato, Superplasticity of TZP/AI2O3 composite, Adv. Ceram. Mater. 3 (1988) 71–76, https://doi.org/10.1111/j.1551-2916.1988.tb00173.x.
[36] Y. Ye, J. Li, H. Zhou, J. Chen, Microstructure and mechanical properties of yttria-stabilized ZrO2/Al2O3 nanocomposite ceramics, Ceram. Int. 34 (2008) 1797–1803, https://doi.org/10.1016/J.CERAMINT.2007.06.005.
[37] R. Lach, K. Wojteczko, A. Dudek, Z. Pedzich, Fracture behaviour of alumina-YAG particulate composites, J. Eur. Ceram. Soc. 34 (2014) 3373–3378, https://doi.org/10.1016/J.JEURCERAMSOC.2014.04.020.
[38] T. Chen, F.A. Mohamed, M.L. Mecartney, Threshold stress superplastic behavior and dislocation activity in a three-phase alumina–zirconia–mullite composite, Acta Mater. 54 (2006) 4415–4426, https://doi.org/10.1016/J.ACTAMAT.2006.05.002.
[39] Y. Zhang, J. Chen, L. Hu, W. Liu, Pressureless-sintering behavior of nanocrystalline ZrO2–Y2O3–Al2O3 system, Mater. Lett. 60 (2006) 2302–2305, https://doi.org/10.1016/J.MATLET.2005.12.129.
[40] J. Pilling, J. Payne, Superplasticity in Al2O3·ZrO2·Al2TiO5 ceramics, Scripta Metall. Mater. 32 (1995) 1091–1097, https://doi.org/10.1016/0956-716X(94)00007-5.
[41] M. Jiménez-Melendo, A. Domínguez-Rodríguez, A. Bravo-León, Superplastic flow of fine-grained yttria-stabilized zirconia polycrystals: constitutive equation and deformation mechanisms, J. Am. Ceram. Soc. 81 (1998) 2761–2776, https://doi.org/10.1111/j.1151-2916.1998.tb02695.x.
[42] D. Ciria, M. Jiménez-Melendo, V. Aubin, G. Dezanneau, High-temperature mechanical behavior of proton-conducting yttrium-doped barium zirconate perovskite, J. Eur. Ceram. Soc. 41 (2021) 1374–1383, https://doi.org/10.1016/j.jeurceramsoc.2020.09.069.
[43] F. Wakai, S. Sakaguchi, Y. Matsuno, Superplasticity of yttria-stabilized tetragonal ZrO2 polycrystals, Adv. Ceram. Mater. 1 (1986) 259–263, https://doi.org/10.1111/j.1551-2916.1986.tb00026.x.

[44] D. Ciria, M. Jiménez-Melendo, V. Aubin, G. Dezanneau, Creep properties of high dense La9.33Si6O26 electrolyte for SOFCs, J. Eur. Ceram. Soc. 40 (2020), https://doi.org/10.1016/j.jeurceramsoc.2020.01.004, 1989–1998.
[45] A.G. Robertson, D.S. Wilkinson, C.H. Caceres, Creep and creep fracture in hot-pressed alumina, J. Am. Ceram. Soc. 74 (1991) 915–921, https://doi.org/10.1111/j.1151-2916.1991.tb04322.x.
[46] R.F. Cook, A.G. Schrott, Calcium segregation to grain boundaries in alumina, J. Am. Ceram. Soc. 71 (1988) 50–58, https://doi.org/10.1111/j.1151-2916.1988.tb05759.x.
[47] N.A. Yahya, R.I. Todd, Influence of C doping on the fracture mode and abrasive wear of Al 2O 3, J. Eur. Ceram. Soc. 32 (2012) 4003–4007, https://doi.org/10.1016/j.jeurceramsoc.2012.07.003.
[48] J. Cho, C.M. Wang, H.M. Chan, J.M. Rickman, M.P. Harmer, Role of segregating dopants on the improved creep resistance of aluminum oxide, Acta Mater. 47 (1999) 4197–4207, https://doi.org/10.1016/S1359-6454(99)00278-5.
[49] J.H. Harding, K.J.W. Atkinson, R.W. Grimes, Experiment and theory of diffusion in alumina, in: J. Am. Ceram. Soc, American Ceramic Society, 2003, pp. 554–559, https://doi.org/10.1111/j.1151-2916.2003.tb03340.x.
[50] A.H. Heuer, Oxygen and aluminum diffusion in α-Al2O3: how much do we really understand? J. Eur. Ceram. Soc. 28 (2008) 1495–1507, https://doi.org/10.1016/j.jeurceramsoc.2007.12.020.
[51] A.A. Sharif, M.L. Mecartney, Superplasticity in cubic yttria-stabilized zirconia with intergranular silica, Acta Mater. 51 (2003) 1633–1639, https://doi.org/10.1016/S1359-6454(02)00564-5.
[52] M. Jiménez-Melendo, H. Haneda, H. Nozawa, Ytterbium cation diffusion in yttrium aluminum garnet (YAG) - implications for creep mechanisms, J. Am. Ceram. Soc. 84 (2001) 2356–2360, https://doi.org/10.1111/j.1151-2916.2001.tb01014.x.
[53] H. Yoshida, Y. Ikuhara, T. Sakuma, High-temperature creep resistance in rare-earth-doped, fine-grained Al2O3, J. Mater. Res. 13 (1998) 2597–2601, https://doi.org/10.1557/JMR.1998.0362.
[54] D. Prot, M. Le Gall, B. Lesage, A.M. Huntz, C. Monty, Self-diffusion in α-Al2O3 IV. Oxygen grain-boundary self-diffusion in undoped and yttria-doped alumina polycrystals, Philos. Mag. A Phys. Condens. Matter, Struct. Defects Mech. Prop 73 (1996) 935–949, https://doi.org/10.1080/01418619608243697.
[55] S. Swaroop, M. Kilo, C. Argirusis, G. Borchardt, A.H. Chokshi, Lattice and grain boundary diffusion of cations in 3YTZ analyzed using SIMS, Acta Mater. 53 (2005) 4975–4985, https://doi.org/10.1016/j.actamat.2005.05.031.
[56] E. Alabort, P. Kontis, D. Barba, K. Dragnevski, R.C. Reed, On the mechanisms of superplasticity in Ti-6Al-4V, Acta Mater. 105 (2016) 449–463, https://doi.org/10.1016/j.actamat.2015.12.003.
[57] R.W. Rice, Evaluation and extension of physical property-porosity models based on minimum solid area, J. Mater. Sci. 31 (1996) 102–118, https://doi.org/10.1007/BF00355133.
[58] D.M. Owen, A.H. Chokshi, Final stage free sintering and sinter forging behavior of a yttria-stabilized tetragonal zirconia, Acta Mater. 46 (1998) 719–729, https://doi.org/10.1016/S1359-6454(97)00105-5.